A Benchmark Study of Different Methods for Calculating One- And Two-Dimensional Optical Spectra

Porscha L. McRobbie and Eitan Geva*

Department of Chemistry and the FOCUS Center, University of Michigan, Ann Arbor, Michigan 48109-1055

Received: June 5, 2009; Revised Manuscript Received: August 4, 2009

The accuracy and robustness of several approximate methods for computing linear and nonlinear optical spectra are considered. The analysis is performed in the context of a benchmark model that consists of a two-state chromophore with shifted harmonic potential surfaces that differ in frequency. The exact one- and two-dimensional spectra for this system are calculated and compared to spectra calculated via the following approximate methods: (1) The semiclassical forward−backward initial-value representation (FB-IVR) method; (2) the linearized semiclassical (LSC) method; (3) the standard second-order cumulant approximation which is based on the ground-state equilibrium frequency−frequency correlation function (2OC); (4) an alternative second-order cumulant approximation which is able to account for nonequilibrium dynamics on the excited-state potential surface (2OCa). All four approximate methods can be shown to reproduce the exact results when the frequencies of the ground and excited harmonic surfaces are identical. However, allowing for the ground and excited surfaces to differ in frequency leads to a more meaningful benchmark model for which none of the four approximate methods is exact. We present a comparison of one- and two-dimensional spectra calculated via the above-mentioned approximate methods to the corresponding exact spectra, as a function of the following parameters: (1) The ratio of excited state to ground-state frequencies; (2) Temperature; (3) The horizontal displacement of the excited-state potential relative to the ground-state potential; (4) The waiting time between the coherence periods in the case of two-dimensional spectra. The FB-IVR method is found to predict spectra which are practically indistinguishable from the exact ones over a wide region of parameter space. The LSC method is found to predict spectra which are in good agreement with the exact ones over the same region of parameter space. The 2OC and 2OCa are found to be highly inaccurate unless the frequencies of the ground and excited states are very similar. These observations give credence to the use of the LSC method for modeling spectra in complex systems, where exact or even FB-IVR-based calculations are prohibitively expensive.

1. Introduction

Multidimensional optical spectroscopy has established itself over the past decade as an extremely powerful and uniquely detailed probe of the structure and dynamics of molecular systems.[1−4] It is also widely accepted that molecularly detailed and dynamically accurate models are necessary in order to take full advantage of these capabilities. However, accomplishing this objective requires overcoming a number of nontrivial theoretical and computational challenges, including the development of self-consistent dynamical methodologies for calculating spectra in complex systems which are both feasible and reliable.

Linear and nonlinear spectra are often expressed in terms of optical response functions (ORFs).[1] However, a quantum-mechanically exact calculation of these ORFs is not feasible in most cases of practical interest. One approach for bypassing this problem is based on a cumulant expansion of the ORFs which is truncated at second order. Within this approach, one may cast the ORFs in terms of equilibrium frequency−frequency correlation functions which are presumably easier to calculate, either fully quantum-mechanically, semiclassically, or classically.

Mixed quantum-classical methods, which are based on treating a small subset of the degrees of freedom (DOF) quantum-mechanically while the rest are treated in a classical-like manner, represent another attractive strategy. However, as is well-known, taking the classical limit of the ORFs with respect to a subset of DOF in a direct manner can lead to expressions which are not unique.[5−11] Several approaches have been proposed in the past for obtaining self-consistent mixed quantum-classical expressions for the ORFs. One such approach is based on linearizing the path-integral forward−backward action associated with the photoinactive DOF with respect to the difference between the forward and backward paths.[9,11−20] Within this approach, one calculates the ORFs by propagating the classical DOF *forward* in time along a classical trajectory that hops between potential surfaces corresponding to various quantum states of the chromophore, as dictated by the Liouville pathway associated with each ORF.[11] In what follows, we will refer to this approach as the *linearized semiclassical* (LSC) method. Another approach is based on replacing the product of quantum propagators that appears in the expressions for the ORFs by a *single* forward−backward semiclassical propagator.[9,11,12,21−27] The partial cancelation of the forward and backward actions usually results in only mildly oscillatory integrands, which makes the calculation of the ORFs more manageable. In what follows, we will refer to this approach as the *forward−backward initial-value-representation* (FB-IVR) method.

* E-mail: eitan@umich.edu.

10.1021/jp905305t CCC: $40.75
Published on Web 09/04/2009

The main goal of the present paper is to provide a meaningful benchmarking of these methods that will aid in assessing their robustness and reliability. To this end, we employ a benchmark model that consists of a two-state chromophore with shifted harmonic potential surfaces. For the sake of concreteness, we will assume that the transition between the two states is electronic. All four approximate methods can be shown to reproduce the exact results when the frequencies of the ground and excited harmonic surfaces are identical. However, allowing for the ground and excited surfaces to differ in frequency leads to a more meaningful benchmark model for which none of the four approximate methods is exact.

We present comparisons of one- and two-dimensional spectra calculated via the above-mentioned approximate methods to the corresponding exact spectra, as a function of various parameters, including the ratio of excited state to ground state frequencies, temperature, the displacement of the excited-state potential relative to the ground-state potential, and the waiting time between the coherence periods in the case of two-dimensional spectra.

The remainder of this paper is organized as follows. In section 2, we present the exact quantum-mechanical expressions for the one- and two-dimensional spectra and formulate the corresponding FB-IVR, LSC, and two distinctly different types of second-order cumulant approximations. The model system is described in section 3, and the results are presented and discussed in section 4. Conclusions and outlook are provided in section 5.

2. Theory

A. Linear and Nonlinear Spectra. We consider a two-state system with the following field-free Hamiltonian:

$$\hat{H} = |\mathrm{g}\rangle\hat{H}_\mathrm{g}\langle\mathrm{g}| + |\mathrm{e}\rangle\hat{H}_\mathrm{e}\langle\mathrm{e}| \tag{1}$$

Here, $|\mathrm{g}\rangle$ and $|\mathrm{e}\rangle$ are the adiabatic ground and excited states of the chromophore and $\hat{H}_{\mathrm{g/e}} = T(\hat{P}) + V_{\mathrm{g/e}}(\hat{Q})$ are the corresponding adiabatic Hamiltonians, where $T(\hat{P})$ and $V_{\mathrm{g/e}}(\hat{Q})$ are the kinetic and potential energy, respectively. For the sake of simplicity, we formulate the different methods for a system with a single photoinactive DOF whose coordinate and momentum operators are given by $\hat{Q}$ and $\hat{P}$, respectively (the extension to the case of multiple photoinactive DOFs is straightforward).[11] It should be noted that eq 1 does not account for nonadiabatic coupling between the adiabatic states, which is justified since population relaxation is often found to be slow relative to dephasing.

The measurement of one-dimensional (1D) spectra is based on detecting the time-resolved linear response of the system to a single impulsive pulse at time $t = 0$. Assuming that the system is in its ground equilibrium state prior to the arrival of the pulse and making the Condon approximation, the signal can be shown to be proportional to the following linear ORF:[1]

$$J(t_1) = |\mu_{\mathrm{ge}}|^2\mathrm{Tr}[e^{i\hat{H}_\mathrm{g}t_1/\hbar}e^{-i\hat{H}_\mathrm{e}t_1/\hbar}\hat{\rho}_\mathrm{g}] \tag{2}$$

Here, the trace is over the photoinactive DOF, μ_{ge} is the transition dipole moment (a constant within the Condon approximation), and $\hat{\rho}_\mathrm{g} = \mathrm{e}^{-\beta\hat{H}_\mathrm{g}}/\mathrm{Tr}[\mathrm{e}^{-\beta\hat{H}_\mathrm{g}}]$ is the equilibrium ground state density operator, with $\beta = 1/k_\mathrm{B}T$. The linear absorption spectrum is then defined as the frequency-domain analogue of $J(t_1)$:[1]

$$I(\omega_1) = \mathrm{Re}\int_0^\infty \mathrm{d}t_1 e^{-i\omega t_1}J(t_1) \tag{3}$$

The measurement of two-dimensional (2D) spectra is often based on detecting the time-resolved nonlinear response of the system to three sequential impulsive pulses with wave vectors $\mathbf{k}_a$, $\mathbf{k}_b$, and $\mathbf{k}_c$. The time delay between pulses a and b is denoted t_1, while that between pulses b and c is denoted t_2. The signal field is detected at a time interval t_3 after pulse c, in the background-free directions $\mathbf{k}_\mathrm{r} = -\mathbf{k}_a + \mathbf{k}_b + \mathbf{k}_c$ and $\mathbf{k}_\mathrm{nr} = \mathbf{k}_a - \mathbf{k}_b + \mathbf{k}_c$, corresponding to the *rephasing* and *nonrephasing* signals, respectively.[3] Assuming once again that the system is in its ground equilibrium state prior to the arrival of the first pulse and making the Condon approximation, the nonrephasing and rephasing signals can be shown to be proportional to the following third-order ORFs:[1]

$$R_\mathrm{nr}(t_3, t_2, t_1) = R_1(t_3, t_2, t_1) + R_4(t_3, t_2, t_1) \tag{4}$$

and

$$R_\mathrm{r}(t_3, t_2, t_1) = R_2(t_3, t_2, t_1) + R_3(t_3, t_2, t_1) \tag{5}$$

respectively. The third-order ORFs $\{R_1,R_2,R_3,R_4\}$ are explicitly given by:[1]

$$\begin{aligned} R_1(t_3, t_2, t_1) &= |\mu_{\mathrm{ge}}|^4\mathrm{Tr}[\mathrm{e}^{i\hat{H}_\mathrm{g}t_1/\hbar}\mathrm{e}^{i\hat{H}_\mathrm{e}t_2/\hbar}\mathrm{e}^{i\hat{H}_\mathrm{g}t_3/\hbar}\mathrm{e}^{-i\hat{H}_\mathrm{e}(t_1+t_2+t_3)/\hbar}\hat{\rho}_\mathrm{g}] \\ &\equiv |\mu_{\mathrm{ge}}|^4F(t_1, t_1 + t_2, t_1 + t_2 + t_3, 0) \end{aligned} \tag{6}$$

$$\begin{aligned} R_2(t_3, t_2, t_1) &= |\mu_{\mathrm{ge}}|^4\mathrm{Tr}[\mathrm{e}^{i\hat{H}_\mathrm{e}(t_1+t_2)/\hbar}\mathrm{e}^{i\hat{H}_\mathrm{g}t_3/\hbar}\mathrm{e}^{-i\hat{H}_\mathrm{e}(t_2+t_3)/\hbar}\mathrm{e}^{-i\hat{H}_\mathrm{g}t_1/\hbar}\hat{\rho}_\mathrm{g}] \\ &\equiv |\mu_{\mathrm{ge}}|^4F(0, t_1 + t_2, t_1 + t_2 + t_3, t_1) \end{aligned} \tag{7}$$

$$\begin{aligned} R_3(t_3, t_2, t_1) &= |\mu_{\mathrm{ge}}|^4\mathrm{Tr}[\mathrm{e}^{i\hat{H}_\mathrm{e}t_1/\hbar}\mathrm{e}^{i\hat{H}_\mathrm{g}(t_2+t_3)/\hbar}\mathrm{e}^{-i\hat{H}_\mathrm{e}t_3/\hbar}\mathrm{e}^{-i\hat{H}_\mathrm{g}(t_1+t_2)/\hbar}\hat{\rho}_\mathrm{g}] \\ &\equiv |\mu_{\mathrm{ge}}|^4F(0, t_1, t_1 + t_2 + t_3, t_1 + t_2) \end{aligned} \tag{8}$$

$$\begin{aligned} R_4(t_3, t_2, t_1) &= |\mu_{\mathrm{ge}}|^4\mathrm{Tr}[\mathrm{e}^{i\hat{H}_\mathrm{g}(t_1+t_2+t_3)/\hbar}\mathrm{e}^{-i\hat{H}_\mathrm{e}t_3/\hbar}\mathrm{e}^{-i\hat{H}_\mathrm{g}t_2/\hbar}\mathrm{e}^{-i\hat{H}_\mathrm{e}t_1/\hbar}\hat{\rho}_\mathrm{g}] \\ &\equiv |\mu_{\mathrm{ge}}|^4F(t_1 + t_2 + t_3, t_1 + t_2, t_1, 0) \end{aligned} \tag{9}$$

where,

$$\begin{aligned} &F(\tau_1, \tau_2, \tau_3, \tau_4) = \\ &\mathrm{Tr}[e^{-i\hat{H}_\mathrm{e}(\tau_1-\tau_2)/\hbar}e^{-i\hat{H}_\mathrm{g}(\tau_2-\tau_3)/\hbar}e^{-i\hat{H}_\mathrm{e}(\tau_3-\tau_4)/\hbar}e^{-i\hat{H}_\mathrm{g}(\tau_4-\tau_1)/\hbar}\hat{\rho}_\mathrm{g}] \end{aligned} \tag{10}$$

Finally, the 2D spectrum at a given value of t_2 is defined as the absorptive part of the frequency-domain analogue, with respect to t_1 and t_3, of $R_\mathrm{nr}(t_3,t_2,t_1)$ and $R_\mathrm{r}(t_3,t_2,t_1)$:[3,28,29]

$$I(\omega_3, t_2, \omega_1) \equiv \mathrm{Re}\int_0^\infty \mathrm{d}t_1 \int_0^\infty \mathrm{d}t_3 \{e^{i(\omega_1 t_1+\omega_3 t_3)} R_{\mathrm{nr}}(t_3, t_2, t_1) + e^{i(-\omega_1 t_1+\omega_3 t_3)} R_{\mathrm{r}}(t_3, t_2, t_1)\} \quad (11)$$

B. The FB-IVR Approximation. Within the FB-IVR approximation, one assumes that the *overall forward−backward time propagators* in eqs 2 and 6−9 can be replaced by the corresponding *single* semiclassical Herman−Kluk propagator,[30,31] so that:[21]

$$J^{\mathrm{FB\text{-}IVR}}(t_1) = |\mu_{\mathrm{ge}}|^2 \frac{1}{2\pi\hbar}\int \mathrm{d}Q_0 \mathrm{d}P_0 D(P_0, Q_0)\langle g_{P_0,Q_0}|\hat{\rho}_{\mathrm{g}}|g_{P_f,Q_f}\rangle e^{iS_J(P_0,Q_0)/\hbar} \quad (12)$$

and

$$R_j^{\mathrm{FB\text{-}IVR}}(t_3, t_2, t_1) = |\mu_{\mathrm{ge}}|^4 \frac{1}{2\pi\hbar}\int \mathrm{d}Q_0 \mathrm{d}P_0 D(P_0, Q_0)\langle g_{P_0,Q_0}|\hat{\rho}_{\mathrm{g}}|g_{P_f,Q_f}\rangle e^{iS_{R_j}(P_0,Q_0)/\hbar} \quad j = 1, 2, 3, 4 \quad (13)$$

Here, $|g_{P_jQ_j}\rangle$ is a coherent state of width γ which is centered at (P_j,Q_j) and corresponds to the wave function

$$\langle Q|g_{P_j,Q_j}\rangle = \left(\frac{\gamma}{\pi}\right)^{1/4}\exp\left(-\frac{1}{2}\gamma(Q - Q_j)^2 + \frac{i}{\hbar}P_j(Q - Q_j)\right) \quad (14)$$

$D(P_0,Q_0)$ is the Herman−Kluk prefactor,

$$D(P_0, Q_0) = \frac{1}{\sqrt{2}}\left(\frac{\partial P_t}{\partial P_0} + \frac{\partial Q_t}{\partial Q_0} - i\hbar\gamma\frac{\partial Q_t}{\partial P_0} + i(\hbar\gamma)^{-1}\frac{\partial P_t}{\partial Q_0}\right)^{1/2} \quad (15)$$

and $\{S_J(P_0,Q_0),S_{R_j}(P_0,Q_0)\}$ are the forward−backward actions which are explicitly given by:

$$S_J(Q_0, P_0) = \int_0^{t_1}\mathrm{d}\tau L_{\mathrm{e}}(Q_\tau, P_\tau) + \int_{t_1}^0 \mathrm{d}\tau L_{\mathrm{g}}(Q_\tau, P_\tau) \quad (16)$$

$$\begin{aligned}
S_{R_1}(Q_0,P_0) &= \int_0^{t_1+t_2+t_3}\mathrm{d}\tau L_{\mathrm{e}}(Q_\tau,P_\tau) + \int_{t_1+t_2+t_3}^{t_1+t_2}\mathrm{d}\tau L_{\mathrm{g}}(Q_\tau,P_\tau) + \int_{t_1+t_2}^{t_1}\mathrm{d}\tau L_{\mathrm{e}}(Q_\tau,P_\tau) + \int_{t_1}^0 \mathrm{d}\tau L_{\mathrm{g}}(Q_\tau,P_\tau)\\
S_{R_2}(Q_0,P_0) &= \int_0^{t_1}\mathrm{d}\tau L_{\mathrm{g}}(Q_\tau,P_\tau) + \int_{t_1}^{t_1+t_2+t_3}\mathrm{d}\tau L_{\mathrm{e}}(Q_\tau,P_\tau) + \int_{t_1+t_2+t_3}^{t_1+t_2}\mathrm{d}\tau L_{\mathrm{e}}(Q_\tau,P_\tau) + \int_{t_1+t_2}^0 \mathrm{d}\tau L_{\mathrm{g}}(Q_\tau,P_\tau)\\
S_{R_3}(Q_0,P_0) &= \int_0^{t_1+t_2}\mathrm{d}\tau L_{\mathrm{g}}(Q_\tau,P_\tau) + \int_{t_1+t_2}^{t_1+t_2+t_3}\mathrm{d}\tau L_{\mathrm{e}}(Q_\tau,P_\tau) + \int_{t_1+t_2+t_3}^{t_1}\mathrm{d}\tau L_{\mathrm{g}}(Q_\tau,P_\tau) + \int_{t_1}^0 \mathrm{d}\tau L_{\mathrm{e}}(Q_\tau,P_\tau)\\
S_{R_4}(Q_0,P_0) &= \int_0^{t_1}\mathrm{d}\tau L_{\mathrm{e}}(Q_\tau,P_\tau) + \int_{t_1}^{t_1+t_2}\mathrm{d}\tau L_{\mathrm{g}}(Q_\tau,P_\tau) + \int_{t_1+t_2}^{t_1+t_2+t_3}\mathrm{d}\tau L_{\mathrm{e}}(Q_\tau,P_\tau) + \int_{t_1+t_2+t_3}^0 \mathrm{d}\tau L_{\mathrm{g}}(Q_\tau,P_\tau)
\end{aligned} \quad (17)$$

where $L_{\mathrm{g/e}}(Q,P) = P\dot{Q} - H_{\mathrm{g/e}}(Q,P)$ is the classical Lagrangian. In the case of the linear ORF, Q_τ and P_τ are calculated along a classical trajectory that starts at Q_0 and P_0 at $\tau = 0$, is propagated forward in time from $\tau = 0$ to $\tau = t_1$ on the excited-state potential, and then backward in time from $\tau = t_1$ to $\tau = 0$ on the ground-state potential (see eq 2). In the case of the third-order ORFs, Q_τ and P_τ are calculated along classical trajectories that start at Q_0 and P_0 at $\tau = 0$, and are propagated forward in time from $\tau = 0$ to $\tau = t_1 + t_2 + t_3$ followed by backward propagation from $\tau = t_1 + t_2 + t_3$ to $\tau = 0$. Importantly, the system hops between the ground and excited potential surfaces throughout this forward−backward time evolution in a manner implied by eqs 6−9. For example, in the case of R_1, the system is propagated on the excited surface from $\tau = 0$ to $\tau = t_1 + t_2 + t_3$, on the ground surface from $\tau = t_1 + t_2 + t_3$ to $\tau = t_1 + t_2$, on the excited surface from $\tau = t_1 + t_2$ to $\tau = t_1$ and finally on the ground surface from $\tau = t_1$ to $\tau = 0$.

C. The LSC Approximation. The LSC approximation is based on writing the ORFs in a path integral form and linearizing the path-integral forward−backward action with respect to the difference between the forward and backward paths.[9,11,13−17,32−34] It should be noted that similar expressions have been previously proposed based on a variety of other semiclassical approaches.[6,35−41] Within this approximation, the linear and third-order ORFs are given by the following expressions:

$$J^{\mathrm{LSC}}(t_1) = |\mu_{\mathrm{ge}}|^2 \frac{1}{2\pi\hbar}\int \mathrm{d}Q_0 \mathrm{d}P_0 \rho_{\mathrm{g,W}}(Q_0, P_0)\exp\{i\int_0^{t_1}\mathrm{d}\tau U(Q_\tau)/\hbar\} \quad (18)$$

and

$$R_j^{\mathrm{LSC}}(t_3, t_2, t_1) = |\mu_{\mathrm{ge}}|^4 \frac{1}{2\pi\hbar}\int \mathrm{d}Q_0 \mathrm{d}P_0 \rho_{\mathrm{g,W}}(Q_0, P_0)\mathrm{e}^{-i\int_0^{t_1}\mathrm{d}\tau U(Q_\tau)/\hbar}\mathrm{e}^{\mp i\int_{t_1}^{t_1+t_2+t_3}\mathrm{d}\tau U(Q_\tau)/\hbar} \quad (19)$$

Here, + and − correspond to rephasing ORFs (R_2,R_3) and nonrephasing ORFs (R_1,R_4), respectively, $\rho_{\mathrm{g},W}(Q,P)$ is the Wigner transform of $\hat{\rho}_{\mathrm{g}}$,

$$\rho_{\mathrm{g,W}}(Q, P) = \int \mathrm{d}\Delta \mathrm{e}^{-iP\Delta/\hbar}\left\langle Q + \frac{\Delta}{2}|\hat{\rho}_{\mathrm{g}}|Q - \frac{\Delta}{2}\right\rangle \quad (20)$$

and $U(Q_\tau)/\hbar$ is the instantaneous value of the transition frequency,

$$U(Q_\tau) = V_{\mathrm{e}}(Q_\tau) - V_{\mathrm{g}}(Q_\tau) \quad (21)$$

Importantly, $\{Q_\tau\}$ are classical trajectories whose initial states are sampled from $\rho_{\mathrm{g},W}(Q_0,P_0)$ and which hop between potential surfaces as they are propagated *forward* from $\tau = 0$ to $\tau = t_1 + t_2 + t_3$ according to the following prescription:

- In the case of J, the propagation takes place on the average potential surface, $V_{\mathrm{ge}} = (V_{\mathrm{g}} + V_{\mathrm{e}})/2$, during $(0,t_1)$.
- In the case of R_1 and R_2, the propagation takes place on V_{ge} during $(0,t_1)$, on the *excited*-state potential surface, V_{e}, during $(t_1,t_1 + t_2)$, and again on V_{ge} during $(t_1 + t_2,t_1 + t_2 + t_3)$.
- In the case of R_3 and R_4, the propagation takes place on V_{ge} during $(0,t_1)$, on the *ground*-state potential surface, V_{g}, during $(t_1,t_1 + t_2)$, and again on V_{ge} during $(t_1 + t_2,t_1 + t_2 + t_3)$.

D. The 2OC Approximation. The 2OC approximation can be derived by taking advantage of the following identity:[1]

$$\exp[i\hat{H}_g t/\hbar]\exp[-i\hat{H}_e t/\hbar] = \exp_+[-i\int_0^t \mathrm{d}t'\hat{U}_g(t')/\hbar] \tag{22}$$

Here, $\exp_+$ corresponds to a positively time-ordered exponential and

$$\hat{U}_g(t) = \exp[i\hat{H}_g t/\hbar]\hat{U}\exp[-i\hat{H}_g t/\hbar] \tag{23}$$

where $\hat{U}/\hbar = [V_e(\hat{Q}) - V_g(\hat{Q})]/\hbar$ is the transition frequency operator.

Substituting eq 22 into eq 2 yields the following expression for the linear ORF:

$$J(t_1) = |\mu_{ge}|^2\mathrm{Tr}\{\exp_+[-i\int_0^{t_1}\mathrm{d}t'\hat{U}_g(t')/\hbar]\hat{\rho}_g\} \equiv |\mu_{ge}|^2\langle\exp_+[-i\int_0^{t_1}\mathrm{d}t'\hat{U}_g(t')/\hbar]\rangle_g \tag{24}$$

Importantly, the initial equilibrium state, $\hat{\rho}_g$, and the dynamics of $\hat{U}_g(t)$ are both governed by the *same* Hamiltonian, $\hat{H}_g$. The 2OC approximation then amounts to replacing $\langle\exp_+[-i\int_0^t\mathrm{d}t'\hat{U}_g(t')/\hbar]\rangle_g$ by the corresponding second-order cumulant expansion:

$$J^{2OC}(t_1) = |\mu_{ge}|^2\exp[-i\langle\hat{U}\rangle_g t_1/\hbar - g(t_1)] \tag{25}$$

Here

$$g(t_1) = \int_0^{t_1}\mathrm{d}\tau(t_1 - \tau)C_g(\tau) \tag{26}$$

where $C_g(\tau)$ is the quantum-mechanical equilibrium ground-state frequency−frequency correlation function:

$$C_g(\tau) = \frac{1}{\hbar^2}[\langle\hat{U}_g(\tau)\hat{U}\rangle_g - \langle\hat{U}\rangle_g^2] \tag{27}$$

Thus, the temporal behavior of the linear ORF within the 2OC approximation reflects equilibrium fluctuations on the ground-state surface. This behavior should be contrasted with the exact expression for $J(t_1)$, eq 2, as well as the corresponding FB-IVR and LSC approximations (eqs 12 and 18, respectively), which are clearly affected by nonequilibrium dynamics on the excited-state surface. The discrepancy can be traced back to the choice of eq 22 as the starting point for the second-order cumulant approximation. As we will show in section E, an alternative and equally valid identity may be used, that leads to an alternative second-order cumulant approximation which is sensitive to nonequilibrium excited-state dynamics.

The 2OC approximations for the third-order ORFs can be obtained in a similar manner. They can be conveniently expressed in terms of $F(\tau_1,\tau_2,\tau_3,\tau_4)$, eq 10, whose 2OC approximation is given by:[1]

$$F^{2OC}(\tau_1,\tau_2,\tau_3,\tau_4) = \mathrm{e}^{i\langle\hat{U}\rangle(-\tau_1+\tau_2-\tau_3+\tau_4)/\hbar}\times \exp\left\{-\frac{1}{\hbar^2}[g(\tau_1-\tau_2) - g(\tau_1-\tau_3) + g(\tau_1-\tau_4) + g(\tau_2-\tau_3) - g(\tau_2-\tau_4) + g(\tau_3-\tau_4)]\right\} \tag{28}$$

Thus, within the 2OC approximation, the temporal behavior of the third-order ORF reflects the very same equilibrium fluctuations on the ground-state surface as the linear ORF.

Finally, it should be noted that truncating the cumulant expansion at second order represents a rather severe approximation which can be expected to further limit the accuracy of the resulting expressions for the ORFs.

E. The 2OCa Approximation. The second-order cumulant expansions in eqs 25 and 28 are not unique. To see this, let us consider an alternative cumulant expansion based on the following identity:

$$\exp[i\hat{H}_g t/\hbar]\exp[-i\hat{H}_e t/\hbar] = \exp_-[-i\int_0^t \mathrm{d}t'\hat{U}_e(t')/\hbar] \tag{29}$$

Here, $\exp_-$ corresponds to a negatively time-ordered exponential and

$$\hat{U}_e(t) = \exp[i\hat{H}_e t/\hbar]\hat{U}\exp[-i\hat{H}_e t/\hbar] \tag{30}$$

Substituting eq 29 into eq 2 then yields the following expression for the linear ORF:

$$J(t_1) = |\mu_{ge}|^2\mathrm{Tr}\{\exp_-[-i\int_0^{t_1}\mathrm{d}t'\hat{U}_e(t')/\hbar]\hat{\rho}_g\} \equiv |\mu_{ge}|^2\langle\exp_-[-i\int_0^{t_1}\mathrm{d}t'\hat{U}_e(t')/\hbar]\rangle_g \tag{31}$$

Importantly, while the initial equilibrium state, $\hat{\rho}_g$, is governed by the ground-state Hamiltonian, the dynamics of $\hat{U}_e(t)$ are governed by the excited-state Hamiltonian.

An alternative second-order cumulant approximation can then be obtained by performing the cumulant expansion of $\langle\exp_-[-i\int_0^t\mathrm{d}t'\hat{U}_e(t')/\hbar]\rangle_g$ and truncating it at second order:

$$J^{2OCa}(t_1) = |\mu_{ge}|^2\exp\left[-\frac{i}{\hbar}\int_0^{t_1}\mathrm{d}t'\langle\hat{U}_e(t')\rangle_g - \frac{1}{\hbar^2}\left\{\int_0^{t_1}\mathrm{d}t''\int_0^{t''}\mathrm{d}t'\langle\hat{U}_e(t')\hat{U}_e(t'')\rangle_g - \frac{1}{2}\left(\int_0^{t_1}\mathrm{d}t'\langle\hat{U}_e(t')\rangle_g\right)^2\right\}\right] \tag{32}$$

It should be emphasized that although the expressions for the linear ORF in eqs 24 and 31 are equivalent, the corresponding second-order cumulant expansions in eqs 25 and 32 are not. More specifically, unlike $\langle\hat{U}\rangle_g/\hbar$ and $C_g(t)/\hbar^2$ which correspond to the averaged transition frequency and fluctuations around it, respectively, at equilibrium on the ground-state surface, the quantities $\langle\hat{U}_e(t')\rangle_g$ and $\langle\hat{U}_e(t')\hat{U}_e(t'')\rangle_g$ reflect the nonequilibrium dynamics of the transition frequency on the excited-state surface and its autocorrelation. In other words, unlike the 2OC approximation, and similarly to the FB-IVR and LSC approximations, the 2OCa ap-

proximation appears to be able to account for the signature of the inherent nonequilibrium excited-state dynamics on the linear ORF.

The 2OCa approximation for $F(\tau_1,\tau_2,\tau_3,\tau_4)$, and thereby the third-order ORFs, can be obtained in a similar manner:

$$F^{2OC}(\tau_1,\tau_2,\tau_3,\tau_4) = \exp[C_1(\tau_1,\tau_2,\tau_3,\tau_4) + C_2(\tau_1,\tau_2,\tau_3,\tau_4)] \quad (33)$$

where $C_1(\tau_1,\tau_2,\tau_3,\tau_4)$ and $C_2(\tau_1,\tau_2,\tau_3,\tau_4)$ are the first- and second-order cumulants, explicitly given by:

$$C_1(\tau_1,\tau_2,\tau_3,\tau_4) = \frac{i}{\hbar}\{-\int_0^{\tau_1} d\tau_1' \langle \hat{U}_e(\tau_1')\rangle_g + \int_0^{\tau_2} d\tau_2' \langle \hat{U}_e(\tau_2')\rangle_g - \int_0^{\tau_3} d\tau_3' \langle \hat{U}_e(\tau_3')\rangle_g + \int_0^{\tau_4} d\tau_4' \langle \hat{U}_e(\tau_4')\rangle_g\} \quad (34)$$

and

$$\begin{aligned} C_2(\tau_1,\tau_2,\tau_3,\tau_4) = -\frac{1}{\hbar^2}\{ &\int_0^{\tau_1} d\tau_1' \int_0^{\tau_1'} d\tau_1'' \langle \hat{U}_e(\tau_1'')\hat{U}_e(\tau_1')\rangle_g + \\ &\int_0^{\tau_2} d\tau_2' \int_0^{\tau_2'} d\tau_2'' \langle \hat{U}_e(\tau_2'')\hat{U}_e(\tau_2')\rangle_g + \\ &\int_0^{\tau_3} d\tau_3' \int_0^{\tau_3'} d\tau_3'' \langle \hat{U}_e(\tau_3'')\hat{U}_e(\tau_3')\rangle_g + \\ &\int_0^{\tau_4} d\tau_4' \int_0^{\tau_4'} d\tau_4'' \langle \hat{U}_e(\tau_4'')\hat{U}_e(\tau_4')\rangle_g + \\ &\int_0^{\tau_1} d\tau_1' \int_0^{\tau_2} d\tau_2' \langle \hat{U}_e(\tau_1')\hat{U}_e(\tau_2')\rangle_g - \\ &\int_0^{\tau_1} d\tau_1' \int_0^{\tau_3} d\tau_3' \langle \hat{U}_e(\tau_1')\hat{U}_e(\tau_3')\rangle_g + \\ &\int_0^{\tau_1} d\tau_1' \int_0^{\tau_4} d\tau_4' \langle \hat{U}_e(\tau_1')\hat{U}_e(\tau_4')\rangle_g + \\ &\int_0^{\tau_2} d\tau_2' \int_0^{\tau_3} d\tau_3' \langle \hat{U}_e(\tau_2')\hat{U}_e(\tau_3')\rangle_g - \\ &\int_0^{\tau_2} d\tau_2' \int_0^{\tau_4} d\tau_4' \langle \hat{U}_e(\tau_2')\hat{U}_e(\tau_4')\rangle_g + \\ &\int_0^{\tau_3} d\tau_3' \int_0^{\tau_4} d\tau_4' \langle \hat{U}_e(\tau_3')\hat{U}_e(\tau_4')\rangle_g\} - \frac{1}{2}C_1^2(\tau_1,\tau_2,\tau_3,\tau_4) \end{aligned} \quad (35)$$

3. Benchmark Model

The main goal of this paper is to provide a systematic analysis of the accuracy of the approximate methods discussed above. To be meaningful, the analysis has to be performed in the context of a benchmark model for which the exact quantum-mechanical ORFs are known and do not coincide with any of the approximations under discussion. A model that satisfies these requirements consists of a two-state chromophore where the ground and excited surfaces are both harmonic, *but differ in frequency*:

$$V_g(\hat{Q}) = \frac{1}{2}\omega_g^2\hat{Q}^2;\ V_e(\hat{Q}) = \hbar\omega_{eg} + \frac{1}{2}\omega_e^2(\hat{Q} + Q_d)^2 \quad (36)$$

Here, ω_g and ω_e are the harmonic frequencies that correspond to the ground and excited surfaces, respectively, Q_d is the horizontal displacement of the excited-state surface relative to the ground-state surface and ω_{eg} is the minimum to minimum transition frequency between the ground state and excited state.

We first consider the special case where $\omega_e = \omega_g$, which corresponds to the one-dimensional version of the popular Brownian oscillator model.[1] As it turns out, this case does not lend itself as a benchmark for the problem at hand. This is because the ground and excited potential surfaces have the exact same shape and therefore induce the same dynamics. As a result, *the linear and third-order ORFs produced via all four approximations (FB-IVR, LSC, 2OC and 2OCa) can be shown to coincide with the exact ones when* $\omega_e = \omega_g$, *regardless of the values of the temperature and horizontal displacement* (see Appendix). Thus, choosing a model system with $\omega_e \neq \omega_g$ is essential for obtaining a meaningful benchmark. It is important to note that the ORFs in the case $\omega_e \neq \omega_g$ differ from those in the case $\omega_e = \omega_g$ in two respects:

• The transition frequency is a quadratic rather than linear function of the coordinate of the photoinactive mode:

$$\hat{U} = \hbar\omega_{eg} + \frac{1}{2}\omega_e^2 Q_d^2 + \omega_e^2 Q_d\hat{Q} + \frac{1}{2}[\omega_e^2 - \omega_g^2]\hat{Q}^2 \quad (37)$$

• The temporal behavior of $\hat{U}(t)$ is sensitive to whether it is governed by the ground or excited-state potential surfaces (which is not the case when $\omega_e = \omega_g$).

The exact quantum-mechanical ORFs when $\omega_e \neq \omega_g$ can be obtained in a variety of ways. For example, the ORFs can be expanded in a basis of vibronic states, such that:

$$J(t_1) = |\mu_{ge}|^2 \sum_{j_0,j_1} P_{gj_0}^{eq} C_{gj_0,ej_1} C_{ej_1,gj_0} \exp[-i\omega_{ej_1,gj_0} t_1] \quad (38)$$

$$\begin{aligned} R_1(t_3,t_2,t_1) &= |\mu_{ge}|^4 \sum_{j_0,j_1,j_2,j_3} P_{gj_0}^{eq} C_{gj_3,ej_1} C_{ej_1,gj_0} C_{gj_0,ej_2} C_{ej_2,gj_3} \times \exp[-i\omega_{ej_1,gj_3} t_3 - i\omega_{ej_1,ej_2} t_2 - i\omega_{ej_1,gj_0} t_1] \\ R_2(t_3,t_2,t_1) &= |\mu_{ge}|^4 \sum_{j_0,j_1,j_2,j_3} P_{gj_0}^{eq} C_{gj_3,ej_2} C_{ej_2,gj_0} C_{gj_0,ej_1} C_{ej_1,gj_3} \times \exp[-i\omega_{ej_2,gj_3} t_3 - i\omega_{ej_2,ej_1} t_2 + i\omega_{ej_1,gj_0} t_1] \\ R_3(t_3,t_2,t_1) &= |\mu_{ge}|^4 \sum_{j_0,j_1,j_2,j_3} P_{gj_0}^{eq} C_{ej_3,gj_0} C_{gj_0,ej_1} C_{ej_1,gj_2} C_{gj_2,ej_3} \times \exp[-i\omega_{ej_3,gj_2} t_3 - i\omega_{gj_0,gj_2} t_2 + i\omega_{ej_1,gj_0} t_1] \\ R_4(t_3,t_2,t_1) &= |\mu_{ge}|^4 \sum_{j_0,j_1,j_2,j_3} P_{gj_0}^{eq} C_{ej_3,gj_2} C_{gj_2,ej_1} C_{ej_1,gj_0} C_{gj_0,ej_3} \times \exp[-i\omega_{ej_3,gj_0} t_3 - i\omega_{gj_2,gj_0} t_2 + i\omega_{ej_3,gj_0} t_1] \end{aligned} \quad (39)$$

Here, $P_{gj}^{eq} = [1 - \exp(-\hbar\omega_g/k_BT)]\exp(-j\hbar\omega_g/k_BT)$ is the equilibrium probability for being in state $|gj\rangle$, $\{|gj\rangle, j = 0,1,2,...\}$ and $\{|ek\rangle, k = 0,1,2,...\}$ are the vibronic states that correspond to the ground and excited states, respectively, $\omega_{aj,bk} = \omega_{eg}[\delta(a,e) - \delta(b,e)] + [(j + 1/2)\omega_a - (k + 1/2)\omega_b]$ are the vibronic transition frequencies, and $C_{ej,gk} \equiv \langle ej|gk\rangle$ are the Franck−Condon coefficients (which can be obtained in closed form in the case of harmonic potentials).

It should be noted that the ORFs in eqs 38 and 39 are purely oscillatory. However, in reality, these ORFs are damped by processes such as electronic dephasing. In order to account for electronic dephasing, we assume that ω_{eg} is a stochastic quantity whose dynamics is uncorrelated with that of the photoinactive mode and can be described as a Gaussian process in the limit of motional narrowing. Within these assumptions, $J(t_1) \rightarrow$

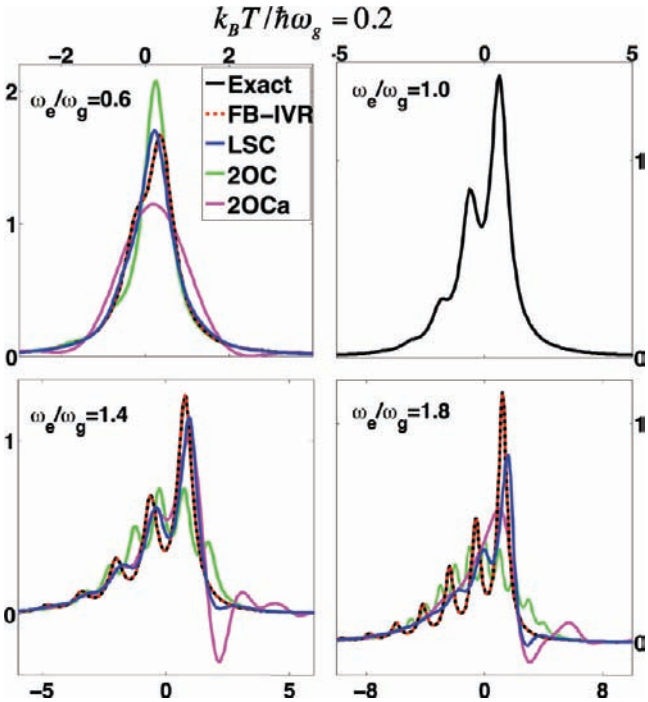

Figure 1. The 1D spectra at $T = 0.2\hbar\omega_g/k_B$ (low temperature) for $Q_d = (\hbar/\omega_g)^{1/2}$ and the following values of ω_e/ω_g: 0.6,1.0,1.4,1.8, as obtained via an exact quantum mechanical calculation, as well as the FB-IVR, LSC, 2OC, and 2OCa approximations.

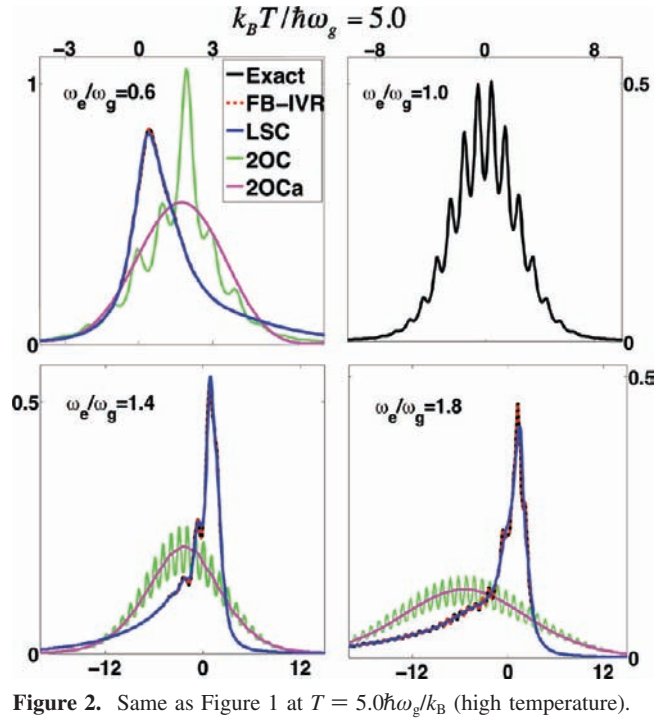

Figure 2. Same as Figure 1 at $T = 5.0\hbar\omega_g/k_B$ (high temperature).

$\exp[-\Gamma t_1]J(t_1)$ and $R_j(t_1,t_2,t_3) \rightarrow \exp[-\Gamma(t_1 + t_3)]R_j(t_1,t_2,t_3)$, where Γ is the electronic dephasing rate constant.

Exact and approximate 1D and 2D spectra were calculated for ω_e/ω_g in the range 0.5−2.0 at $T = 0.2\hbar\omega_g/k_B$ (low temperature) and $T = 5.0\hbar\omega_g/k_B$ (high temperature) and for different values of the horizontal displacement $Q_d/(\hbar/\omega_g)^{1/2} =$ 0.5,1.0,1.5. The 2D spectra were also calculated at different values of t_2. The electronic dephasing rate constant used in all calculations was $\Gamma = \omega_g/2.8$ and the spectra are presented so that the frequency origin is set at $\langle\omega_{eg}\rangle$, which corresponds to the average of the stochastic $\omega_{eg}(t)$.

4. Results

A. 1D Spectra. The 1D spectra at $T = 0.2\hbar\omega_g/k_B$ (low temperature) and $T = 5.0\hbar\omega_g/k_B$ (high temperature) are shown in Figures 1 and 2, respectively, for $Q_d = (\hbar/\omega_g)^{1/2}$ and the following four representative values of ω_e/ω_g: 0.6,1.0,1.4,1.8. As expected, the quantum-mechanically exact 1D spectra consist of peaks at the various vibronic transition frequencies. The widths of these peaks are determined by Γ, and their intensities are determined by the thermal weight of the initial state and the corresponding products of Franck−Condon coefficients (see eq 38). The following observations can be made based on these results:

• The 1D spectra obtained via FB-IVR are found to be in excellent agreement with the exact results throughout the entire region of parameter space considered. It should be noted that the fact that the coherent state width parameter γ was chosen to be constant (see eq 14) implies that FB-IVR is not exact for the system considered here. More specifically, by assuming that γ is constant, FB-IVR neglects the fact that what is a coherent state on one surface corresponds to a squeezed state on the other surface. However, the corresponding changes of the width do not seem to affect the 1D spectra in a noticeable way even when ω_e and ω_g are significantly different.

• Although LSC is not as accurate as FB-IVR, it is clearly able to reproduce the main features of the 1D spectra rather well throughout a wide region of parameter space and improves with increasing temperature. It should be noted that the agreement between the LSC and exact results depends on the choice of electronic dephasing rate constant, Γ. More specifically, the LSC approximation is known to be overdamped in comparison to the corresponding fully quantum-mechanical results, which can be attributed to the fact that it is based on purely classical all-forward dynamics and therefore lacks the ability to account for coherent quantum dynamical effects.[12,16,42] As a result, the LSC approach is particularly suitable for modeling spectra in cases where the physical dephasing is faster than any nonphysical dephasing caused by this overdamping. This is often the case in systems of practical interest and under ambient conditions. In order to mimic this situation, we have used in the present study a large enough value of Γ so that the damping of the ORFs is dominated by it, rather than by the nonphysical dephasing inherent to the LSC approximation.

• Although the 1D spectra obtained via 2OC coincide with the exact ones when $\omega_e = \omega_g$, the agreement between them deteriorates rather rapidly once ω_e is allowed to deviate from ω_g. Importantly, the deviations are qualitative in nature in the sense that 2OC is unable to reproduce the overall asymmetry of the spectrum as well as the locations, relative intensities, and widths of the peaks. These deviations reflect the two major approximations underlying 2OC, namely that the spectra reflect equilibrium ground-state dynamics *and* that this equilibrium dynamics can be described by a Gaussian process.

• The 1D spectra obtained via 2OCa coincide with the exact spectra and the spectra obtained via 2OC when $\omega_e = \omega_g$. However, the 2OCa-based spectra are seen to deviate significantly from both when ω_e differs from ω_g. At low temperatures, 2OCa appears to be somewhat better at predicting the peak locations, which can be attributed to its ability to account for at least some of the spectral signature of nonequilibrium excited-state dynamics on the spectra. Unfortunately, the low-temperature 2OCa-based spectra also become pronouncedly negative in some regions, which is clearly nonphysical. At high temper-

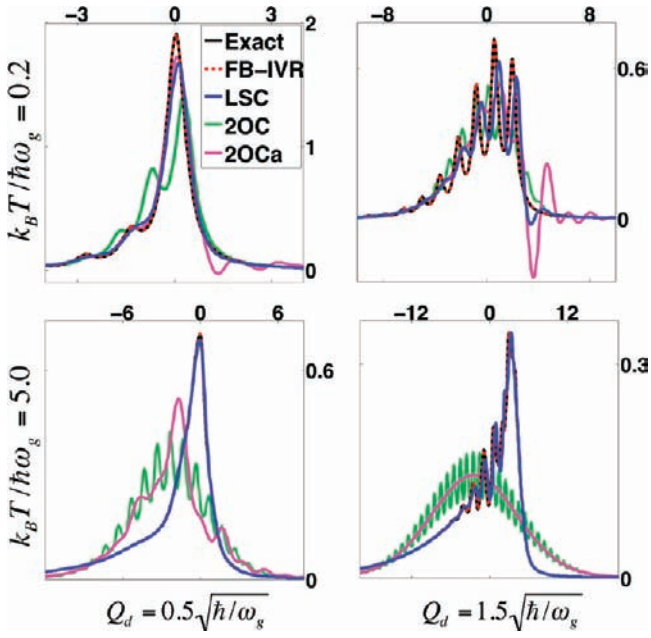

Figure 3. 1D spectra for $Q_d = (0.5,1.5)(\hbar/\omega_g)^{1/2}$, $\omega_e/\omega_g = 1.4$ and at $T = 0.2\hbar\omega_g/k_B$ and $T = 5.0\hbar\omega_g/k_B$, as obtained via an exact quantum mechanical calculation, as well as the FB-IVR, LSC, 2OC, and 2OCa approximations.

atures, the spectra obtained via 2OCa are seen to coincide with the envelopes of the spectra obtained via 2OC but lack the fine structure of the latter, which can be attributed to overdamping generated by the nonequilibrium excited-state dynamics. Finally, the fact that the accuracy of two distinctly different second-order cumulant approximations deteriorate so rapidly once we allow ω_e to differ from ω_g suggests that this type of approximation can only be expected to be reliable within a rather narrow region of parameter space.

In Figure 3, we show the 1D spectra for two other values of Q_d, namely $Q_d = (0.5,1.5)(\hbar/\omega_g)^{1/2}$, in the case $\omega_e/\omega_g = 1.4$ and at $T = 0.2\hbar\omega_g/k_B$ and $T = 5.0\hbar\omega_g/k_B$. It should be noted that the 1D spectra obtained via all four approximate methods coincide with the exact ones when $\omega_e = \omega_g$, regardless of the value of Q_d. However, this is not the case when $\omega_e/\omega_g \neq 1$. The 1D spectra obtained via FB-IVR are seen to be in excellent agreement with the exact ones regardless of the value of Q_d. As expected, LSC also remains accurate at high temperature regardless of the value of Q_d. Interestingly, LSC is also observed to remain rather accurate even at the lower temperature, although the level of accuracy is observed to diminish with increasing Q_d. Finally, the 1D spectra predicted by 2OC and 2OCa are seen to be significantly different from the exact ones regardless of the values of Q_d, and the deviations are seen to *increase* with temperature.

B. 2D Spectra. The exact 2D spectra at $T = 0.2\hbar\omega_g/k_B$ (low temperature) and $T = 5.0\hbar\omega_g/k_B$ (high temperature) are shown in Figure 4 as a function of t_2, for $Q_d = (\hbar/\omega_g)^{1/2}$ and in the special case where the frequencies of the ground and excited surfaces coincide, namely $\omega_e = \omega_g$. As expected, the 2D spectra consist of peaks at the various vibronic frequencies. The widths of these peaks are determined by Γ, and their intensities are determined by the thermal weight of the initial state and the products of Franck−Condon coefficients (see eq 39). The peak pattern is also seen to change as a function of t_2 as dictated by eq 39, and the number of peaks is seen to increase with temperature, which reflects the larger number of initially populated ground vibronic states. However, the fact that the

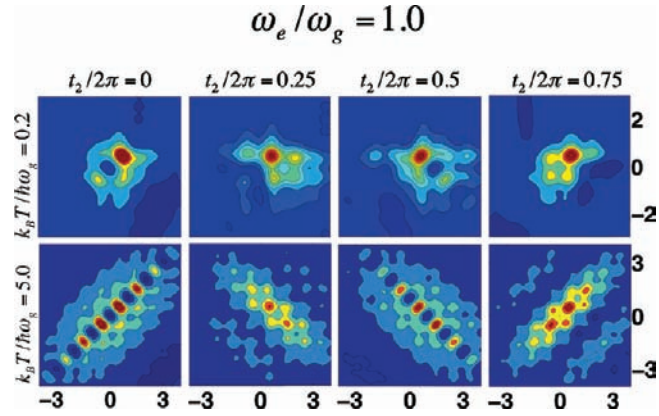

Figure 4. The exact 2D spectra at $T = 0.2\hbar\omega_g/k_B$ (low temperature) and $T = 5.0\hbar\omega_g/k_B$ (high temperature) as a function of t_2, for $Q_d = (\hbar/\omega_g)^{1/2}$ and $\omega_e/\omega_g = 1$.

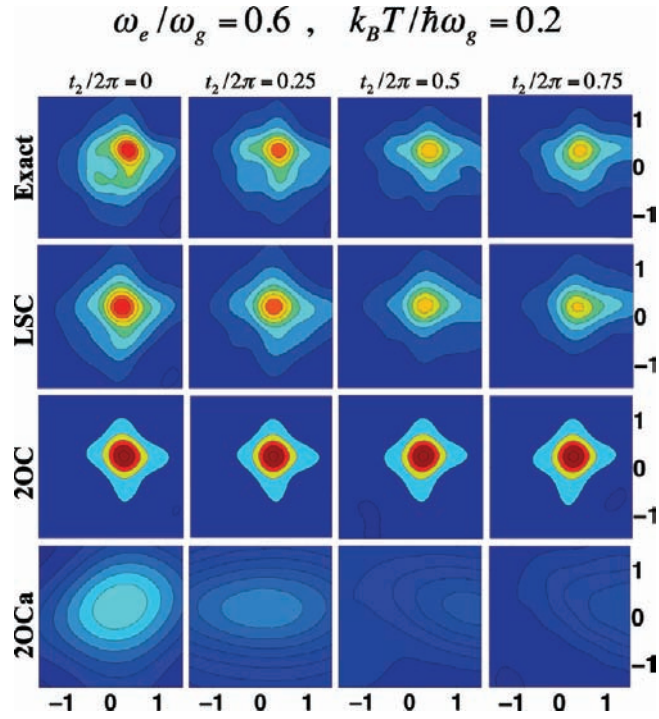

Figure 5. A comparison of the exact 2D spectra to the corresponding LSC, 2OC, and 2OCa approximations in the case where $\omega_e/\omega_g = 0.6$ at $T = 0.2\hbar\omega_g/k_B$ (low temperature).

vibronic wave functions become increasingly more localized at the turning points with increasing energy implies that the corresponding Franck−Condon coefficients drop rapidly. As a result, the intensity of peaks that correspond to transitions between excited states tends to rapidly decrease the more excited the vibronic states are. As for the 1D spectra, the 2D spectra generated via FB-IVR, LSC, 2OC, and 2OCa all coincide with the exact results when $\omega_e = \omega_g$ (see Figure 4).

In Figures 5−10, we present a comparison of the exact 2D spectra to the corresponding LSC, 2OC, and 2OCa approximations in the case where $\omega_e \neq \omega_g$. More specifically, we compare 2D spectra at $T = 0.2\hbar\omega_g/k_B$ (Figures 5−7) and $T = 5.0\hbar\omega_g/k_B$ (Figures 8−10) for $Q_d = (\hbar/\omega_g)^{1/2}$ and at various values of t_2. We have also repeated the calculation for other values of Q_d (not shown). However, we have not found new trends with respect to the Q_d dependence besides those already noted in the context of the 1D spectra (see Figure 3). The 2D spectra generated via FB-IVR were observed to be practically indistinguishable from the exact ones and are therefore not shown.

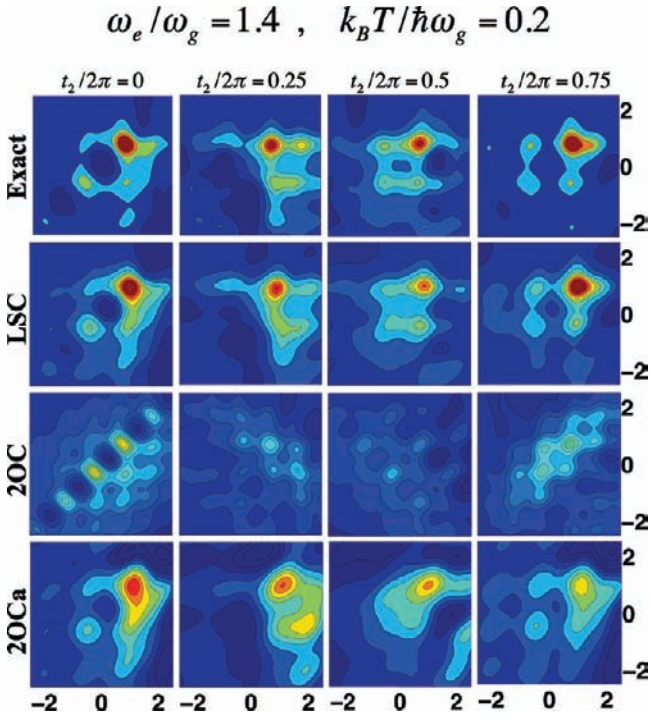

Figure 6. A comparison of the exact 2D spectra to the corresponding LSC, 2OC, and 2OCa approximations in the case where $\omega_e/\omega_g = 1.4$ at $T = 0.2\hbar\omega_g/k_B$ (low temperature).

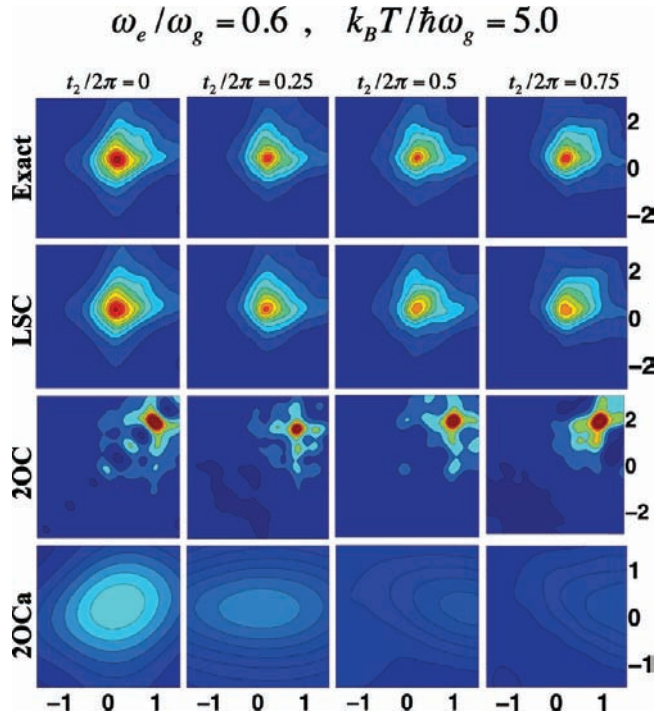

Figure 8. A comparison of the exact 2D spectra to the corresponding LSC, 2OC, and 2OCa approximations in the case where $\omega_e/\omega_g = 0.6$ at $T = 5.0\hbar\omega_g/k_B$ (high temperature).

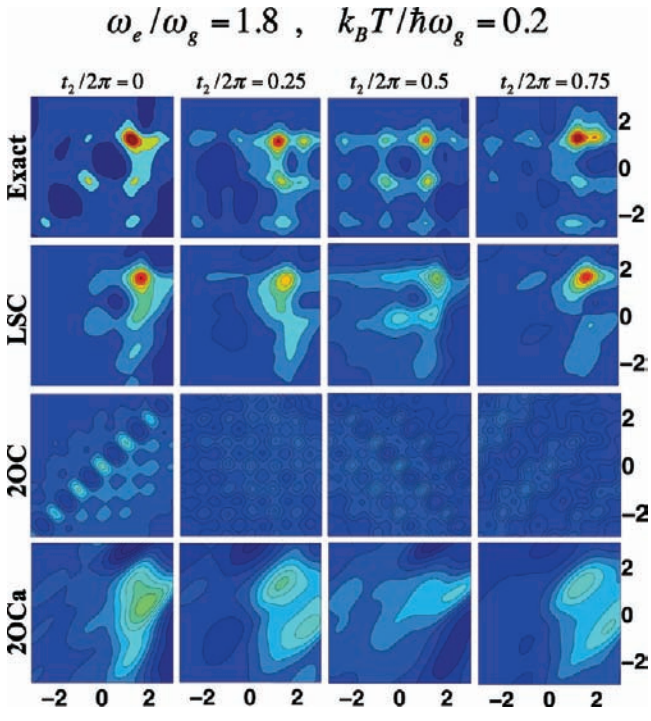

Figure 7. A comparison of the exact 2D spectra to the corresponding LSC, 2OC, and 2OCa approximations in the case where $\omega_e/\omega_g = 1.8$ at $T = 0.2\hbar\omega_g/k_B$ (low temperature).

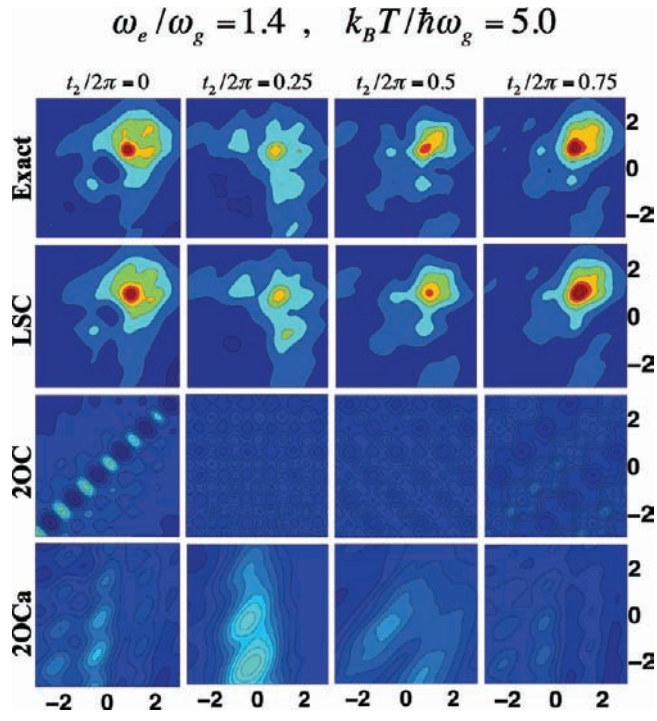

Figure 9. A comparison of the exact 2D spectra to the corresponding LSC, 2OC, and 2OCa approximations in the case where $\omega_e/\omega_g = 1.4$ at $T = 5.0\hbar\omega_g/k_B$ (high temperature).

This implies that although strictly speaking the FB-IVR approximation is not exact when $\omega_e \neq \omega_g$, the 2D spectra are essentially insensitive to the difference, at least for the model under consideration here.

Unlike the spectra generated via FB-IVR, there are visible deviations between the exact spectra and those obtained via LSC. However, those deviations remain small throughout the region of parameter space considered, thereby testifying to the robustness of the LSC approximation. In fact, while the accuracy of the LSC approximation at the high temperature is expected in light of the classical treatment of the photoinactive coordinate, the fact that it is also accurate at the low temperature is somewhat surprising. The latter observation can probably be attributed to the fact that all the potential energy surfaces involved are harmonic, as the presence of anharmonicities would have given rise to more pronounced quantum effects at low

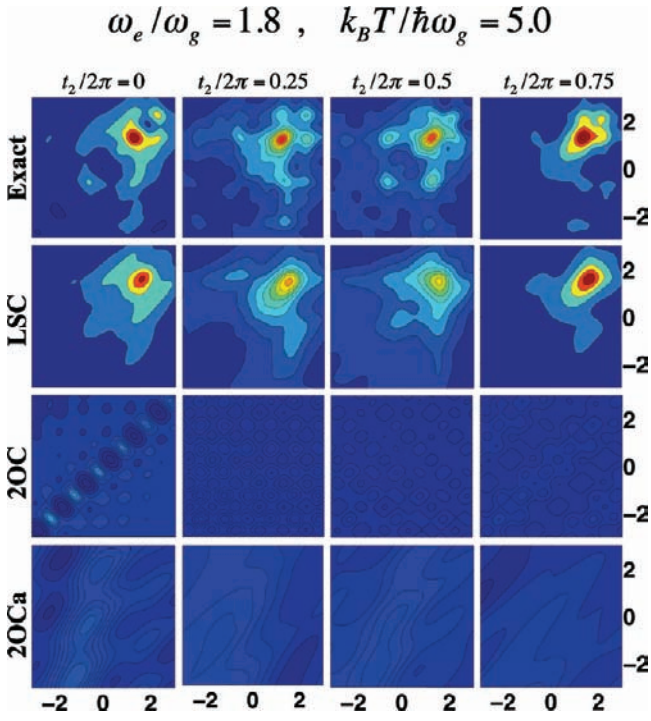

Figure 10. A comparison of the exact 2D spectra to the corresponding LSC, 2OC, and 2OCa approximations in the case where $\omega_e/\omega_g = 1.8$ at $T = 5.0\hbar\omega_g/k_B$ (high temperature).

temperatures. It should also be noted that the accuracy of LSC is better at $\omega_e/\omega_g < 1$, compared to $\omega_e/\omega_g > 1$, since the lower frequency of the excited-state surface makes it more classical.

Finally, the 2D spectra generated via 2OC and 2OCa are seen to be highly inaccurate in almost every respect. More specifically, although the 2D spectra generated by both the 2OC and 2OCa approximations coincide with the exact ones when $\omega_e = \omega_g$, the agreement between the approximate and exact spectra deteriorates rather rapidly once ω_e is allowed to differ from ω_g. At the high temperature, the predictions of 2OC and 2OCa are seen to differ qualitatively from the exact results regardless of the value of ω_e/ω_g. However, at the lower temperature, 2OC actually seems to perform reasonably well for $\omega_e/\omega_g = 0.6$, while 2OCa fails. Nevertheless, the trend reverses for $\omega_e/\omega_g = 1.4$, where it is actually 2OCa which is seen to be in reasonable agreement with the exact results, while 2OC fails. This suggests the growing importance of accounting for excited-state dynamics when $\omega_e > \omega_g$, at least at low temperatures. However, generally speaking, the second-order cumulant approximation, in either its 2OC or 2OCa renditions, is seen to be rather inaccurate and to lack robustness even in the case where the potential surfaces are harmonic, provided that they do not have the same frequency.

5. Conclusions

In this paper, we have considered the accuracy of the FB-IVR, LSC, 2OC, and 2OCa methods for calculating 1D and 2D spectra within the context of a benchmark model of a two-state chromophore with shifted harmonic potential surfaces. We have shown that all methods reproduce spectra that coincide with the exact ones when the frequencies of the two surfaces are the same, regardless of the temperature or relative displacement of those surfaces. As a result, a meaningful benchmark must be based on having the two surfaces correspond to different frequencies, and the accuracy consequently becomes dependent on the frequency ratio.

The spectra generated via FB-IVR were found to be in excellent agreement with the exact ones throughout the entire region of parameter space considered. We have also observed good agreement between the spectra calculated via LSC and the exact ones, provided that the exact ORFs decay on a time scale shorter than that of the nonphysical overdamping inherent to the LSC approximation. Finally, the second-order cumulant approximation, either in its standard form, 2OC, or alternative form, 2OCa, were generally found to be inaccurate and unreliable unless $\omega_e \approx \omega_g$.

Although the FB-IVR method is superior to LSC in regard to accuracy, its computational cost is also significantly higher. Thus, our results seem to point to LSC as the method of choice for modeling 2D spectra in complex systems for which an exact quantum-mechanical, or even the approximate but rather expensive FB-IVR method, may not be feasible. Applications of LSC to model spectra in complex systems such as hydrogen-bonded liquid solutions have been reported in a separate paper.[43]

Acknowledgment. E.G. is grateful to the National Science Foundation (Grant No. CHE-0809506) and the Petroleum Research Fund for financial support.

Appendix: Linear Response in the Same-Frequency Case

In this appendix, we show that FB-IVR, LSC, 2OC, and 2OCa all reproduce the exact 1D spectra when $\omega_e = \omega_g \equiv \omega$. We start out by noting that in this case, the transition frequency is linear in $\hat{Q}$ (see eq 37): $\hat{U} = \hbar\omega_{eg}^{v} + (2S)^{1/2}\hbar\omega\hat{Q} \equiv \hbar\omega_{eg}^{v} + \delta\hat{U}$, where $\omega_{eg}^{v} = \omega_{eg} + \omega S$ is the vertical transition frequency, $\delta\hat{U} \equiv (2S)^{1/2}\hbar\omega\hat{Q}$ is the fluctuation relative to it, and $S \equiv \omega Q_d^2/2\hbar$ is the Huang−Rhys factor. In the Heisenberg picture, $\delta\hat{U}_{g/e}(t) = (2S)^{1/2}\hbar\omega\hat{Q}_{g/e}(t)$, where $\hat{Q}_{g/e}(t)$ is obtained by solving the Heisenberg equations for the position operator on the ground and excited potential surfaces:

$$\hat{Q}_g(t) = \hat{Q}\cos(\omega t) + \frac{\hat{P}}{\omega}\sin(\omega t) \tag{A1}$$

$$\hat{Q}_e(t) = -Q_d + (\hat{Q} - Q_d)\cos(\omega t) + \frac{\hat{P}}{\omega}\sin(\omega t) \tag{A2}$$

As is well-known, the 2OC approximation reproduces the exact result when $\omega_e = \omega_g$:[1]

$$J(t_1) = J^{2OC}(t_1) = |\mu_{ge}|^2\exp\left\{-i\omega_{eg}^{v}t_1 - S\left[\coth\left(\frac{\beta\hbar\omega}{2}\right)(1 - \cos(\omega t_1)) + i(\sin(\omega t_1) - \omega t_1)\right]\right\} \tag{A3}$$

However, it can also be shown that, in this case, $J^{2OCa}(t_1)$ coincides with $J^{2OC}(t_1)$ and hence the exact result. To this end, it can be easily verified that

$$\langle\delta\hat{U}_e(t)\rangle_g = -2\hbar\omega S[1 - \cos(\omega t)] \tag{A4}$$

and

$$\langle \delta\hat{U}_e(t')\delta\hat{U}_e(t'')\rangle_g = 2S\hbar^2\omega^2\{2S[1 - \cos(\omega t') - \cos(\omega t'') + \cos(\omega t')\cos(\omega t'')] + \frac{1}{2}\coth\left(\frac{\beta\hbar\omega}{2}\right)[\cos(\omega t')\cos(\omega t'') + \sin(\omega t')\sin(\omega t'')] + \frac{i}{2}[\cos(\omega t')\sin(\omega t'') - \sin(\omega t')\cos(\omega t'')] \quad \text{(A5)}$$

Upon substitution of eqs A4 and A5 into eq 32, performing the integrals explicitly and rearranging, one finds that $J^{2OCa}(t_1)$ indeed reduces to eq A3.

The FB-IVR approximation is exact when $\omega_e = \omega_g$ since the two surfaces share the same set of coherent states. More specifically, starting with a coherent wave packet on the ground-state potential surface guarantees that it will remain coherent even after hopping to the excited-state potential energy surface, thereby reproducing the exact result.

Although less obvious, the LSC approximation also turns out to be exact when $\omega_e = \omega_g$. This can be verified explicitly by substituting the well-known expression for the Wigner distribution that corresponds to thermal equilibrium on the ground-state harmonic potential surface,[44]

$$\rho_{g,W}(Q_0, P_0) = \frac{1}{\pi\hbar}\tanh\left(\frac{\beta\hbar\omega}{2}\right)\exp\left\{-\frac{2}{\hbar\omega}\tanh\left(\frac{\beta\hbar\omega}{2}\right)\left[\frac{P_0^2}{2} + \frac{1}{2}\omega^2 Q_0^2\right]\right\} \quad \text{(A6)}$$

into eq 18, and solving for Q_τ on the average potential energy surface, $V_{ge}(Q) = (1/2)\omega^2(Q + Q_d/2)^2 + \text{constant}$, so that

$$\int_0^{t_1} d\tau \delta U(Q_\tau) = Q_d Q_0 \omega \sin(\omega t_1) + Q_d P_0[1 - \cos(\omega t_1)] - S[\omega t_1 - \sin(\omega t_1)] \quad \text{(A7)}$$

Substitution of eqs A6 and A7 into eq 18 followed by explicit integration over Q_0 and P_0 is then found to reproduce the exact $J(t_1)$, eq A3, thereby implying that the linearization of the forward−backward action is exact when $\omega_e = \omega_g$.

Finally, although the derivation is significantly more cumbersome, it can be similarly shown that, in the case $\omega_e = \omega_g$, FB-IVR, LSC, 2OC, and 2OCa all reproduce the exact third-order ORFs, $\{R_1,R_2,R_3,R_4\}$, that underly the 2D spectra. It should also be pointed out that FB-IVR, LSC, 2OC still produce the exact linear and nonlinear ORFs when the model is extended to include an arbitrary number of independent harmonic photoinactive modes (which is equivalent to the popular Brownian oscillator model).[1]

References and Notes

(1) Mukamel, S. *Principles of Nonlinear Optical Spectroscopy*; Oxford: New York, 1995.
(2) Jonas, D. M. *Annu. Rev. Phys. Chem.* **2003**, *54*, 425.
(3) Khalil, M.; Demirodoven, N.; Tokmakoff, A. *J. Phys. Chem. A* **2003**, *107*, 5258.
(4) Cho, M. *Chem. Rev.* **2008**, *108*, 1331.
(5) Mukamel, S. *J. Chem. Phys.* **1982**, *77*, 173.
(6) Shemetulskis, N. E.; Loring, R. F. *J. Chem. Phys.* **1992**, *97*, 1217.
(7) Saven, J. G.; Skinner, J. L. *J. Chem. Phys.* **1993**, *99*, 4391.
(8) Stephens, M. D.; Saven, J. G.; Skinner, J. L. *J. Chem. Phys.* **1997**, *106*, 2129.
(9) Shi, Q.; Geva, E. *J. Chem. Phys.* **2005**, *122*, 064506.
(10) Ka, B. J.; Geva, E. *J. Chem. Phys.* **2006**, *125*, 214501.
(11) Shi, Q.; Geva, E. *J. Chem. Phys.* **2008**, *129*, 124505.
(12) Miller, W. H. *J. Chem. Phys.* **2006**, *125*, 132305.
(13) Shi, Q.; Geva, E. *J. Chem. Phys.* **2003**, *118*, 8173.
(14) Shi, Q.; Geva, E. *J. Phys. Chem. A* **2003**, *107*, 9059.
(15) Shi, Q.; Geva, E. *J. Phys. Chem. A* **2003**, *107*, 9070.
(16) Shi, Q.; Geva, E. *J. Phys. Chem. A* **2004**, *108*, 6109.
(17) Poulsen, J. A.; Nyman, G.; Rossky, P. J. *J. Chem. Phys.* **2003**, *119*, 12179.
(18) Liu, J.; Miller, W. H. *J. Chem. Phys.* **2006**, *125*, 224104.
(19) Liu, J.; Miller, W. H. *J. Chem. Phys.* **2006**, *127*, 114506.
(20) Liu, J.; Miller, W. H. *J. Chem. Phys.* **2006**, *128*, 144511.
(21) Makri, N.; Thompson, K. *Chem. Phys. Lett.* **1998**, *291*, 101.
(22) Thompson, K.; Makri, N. *J. Chem. Phys.* **1999**, *110*, 1343.
(23) Kühn, O.; Makri, N. *J. Phys. Chem. A* **1999**, *103*, 9487.
(24) Sun, X.; Miller, W. H. *J. Chem. Phys.* **1999**, *110*, 6635.
(25) Sepúlveda, M. A.; Mukamel, S. *J. Chem. Phys.* **1995**, *102*, 9327.
(26) Spencer, C. F.; Loring, R. F. *J. Chem. Phys.* **1996**, *105*, 6596.
(27) Ovchinnikov, M.; Apkarian, V. A.; Voth, G. A. *J. Chem. Phys.* **2001**, *184*, 7130.
(28) Schmidt, J. R.; Corcelli, S. A.; Skinner, J. L. *J. Chem. Phys.* **2005**, *123*, 044513.
(29) Khalil, M.; Demirodoven, N.; Tokmakoff, A. *J. Phys. Chem. A* **2003**, *107*, 5258.
(30) Herman, M. F.; Kluk, E. *Chem. Phys.* **1984**, *91*, 27.
(31) Kluk, E.; Herman, M. F.; Davis, H. L. *J. Chem. Phys.* **1986**, *84*, 326.
(32) Shi, Q.; Geva, E. *J. Chem. Phys.* **2004**, *120*, 10647.
(33) Ka, B. J.; Shi, Q.; Geva, E. *J. Phys. Chem. A* **2005**, *109*, 5527.
(34) Ka, B. J.; Geva, E. *J. Phys. Chem. A* **2006**, *110*, 9555.
(35) Wang, H.; Sun, X.; Miller, W. H. *J. Chem. Phys.* **1998**, *108*, 9726.
(36) Sun, X.; Miller, W. H. *J. Chem. Phys.* **1997**, *106*, 916.
(37) Sun, X.; Wang, H.; Miller, W. H. *J. Chem. Phys.* **1998**, *109*, 4190.
(38) Sun, X.; Wang, H.; Miller, W. H. *J. Chem. Phys.* **1998**, *109*, 7064.
(39) Wang, H.; Song, X.; Chandler, D.; Miller, W. H. *J. Chem. Phys.* **1999**, *110*, 4828.
(40) Miller, W. H. *J. Phys. Chem. A* **1999**, *103*, 9384.
(41) Shao, J. S.; Liao, J. L.; Pollak, E. *J. Chem. Phys.* **1998**, *108*, 9711.
(42) Egorov, S. A.; Rabani, E.; Berne, B. J. *J. Chem. Phys.* **1998**, *108*, 1407.
(43) Hanna, G.; Geva, E. *J. Phys. Chem. B* **2009**, *113*, 9278.
(44) Hillery, M.; O'Connell, R. F.; Scully, M. O.; Wigner, E. P. *Phys. Rep.* **1984**, *106*, 121.

JP905305T